Chapter 6

Piezoelectric MEMS Power Generators for Vibration Energy Harvesting

Wen Jong Wu and Bor Shiun Lee

Additional information is available at the end of the chapter

http://dx.doi.org/10.5772/51997

1. Introduction

1.1. Background

Over the past few years, the development of wireless sensor network application has generated much interest. Research on the various ways to power wireless sensor devices has gradually become important [1-3]. Unlike portable devices such as cell phones and PDAs where the batteries can be recharged or replaced regularly, most micro sensors are powered by embedded batteries. Therefore, the life of a battery is a major constraint when trying to extend the convenience of micro sensors. With the advent of low-power electronic designs and improvements in fabrication, technology has progressed towards the possibility of self-powered sensor nodes and micro sensors [4].

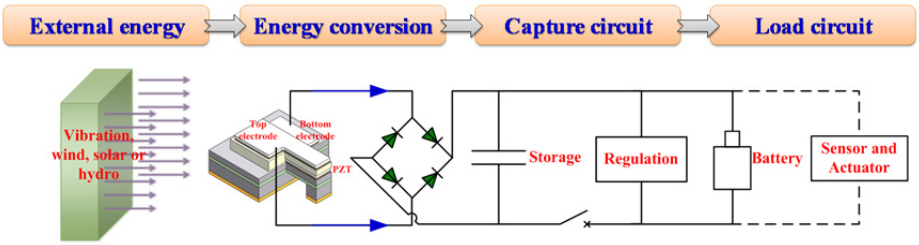

Figure 1. Schematic diagram of a typical power harvesting system

Figure 1 shows a typical power harvesting system for self-powered sensor nodes and micro sensors. It includes an external energy source, a transducer to convert energy from external energy to electric power, a harvesting circuit to optimize the harvesting efficiency and a storage battery or a load circuit. Much research has been focused on harvesting electric power from various ambient energy sources, including solar power, thermal gradients and

INTECH
open science | open minds

© 2012 Wu and Lee, licensee InTech. This is an open access chapter distributed under the terms of the Creative Commons Attribution License (http://creativecommons.org/licenses/by/3.0), which permits unrestricted use, distribution, and reproduction in any medium, provided the original work is properly cited.

Energy Source	Power Density	Energy Density
Batteries (znic-air)		1050-1560mWh/cm^3
Batteries (rechargeable lithium)		300 mWh/cm^3 (3-4V)
Solar (outdoors)	15mW/cm^2 (direct sun) 0.15mW/cm^2 (cloudy day)	
Solar (indoors)	0.006 mW/cm^2 (standard office desk) 0.057 mW/cm^2(<60W desk lamp)	
Vibrations	0.01-0.1 mW/cm^3	
Acoustic Noise	3E-6 mW/cm^2 at 75 dB 9.6E-4 mW/cm^2 at 100 dB	
Passive Human-Powered Systems	1.8mW (shoe inserts)	
Nuclear Reaction	80 mW/cm^3	1E6mWh/cm^3

Table 1. A comparison of energy sources [2] [1]

vibrations [5]. When comparing all possible energy sources, mechanical vibration is a potential power source that can be easily accessed through adopting micro-electromechanical systems (MEMS) technology [6, 7]. Table 1 shows a comparison of various energy sources [2]. Mechanical vibration energy can be converted into usable electrical energy through piezoelectric [3, 8, 9], electromagnetic [4, 10, 11] and electrostatic [12-14] transducers. The piezoelectric transducer is considered a potential choice when compared with electromagnetic and electrostatic transducers due to its high energy density [15]. Such comparison is given in table 2. [2]

Type	Energy Density (mJ cm^{-3})	Equation	Assumptions
Piezoelectric	35.4	$(1/2)\sigma_y^2 k^2/2c$	PZT 5H
Electromagnetic	24.8	$(1/2)B^2/\mu_0$	0.25 T
Electrostatic	4	$(1/2)\varepsilon_0 E^2$	3 x 10^7 V m^{-1}

Table 2. Summary of maximum energy densities of three kinds of transducers [15]

1.2. Literature review

Several researches have been focused on the piezoelectric power generators for vibration power harvesting. T. Starner [16] et. al have concluded that power generation through walking can easily generate power when needed, and 5–8W of power may be recovered

[1] Values are estimates from literatures, analyses and few experiments; Values are highly dependent on amplitude and frequency of the driving vibrations

[2] There were already many successful vibration harvesting devices reported of different structures and interface circuits [7, 16, 17]. Piezoelectric material that has been found to have the ability to convert vibration energy to electric power has sparked much attention as it was attractive for use in MEMS applications [16, 18, 19, 20, 21, 22].

while walking at a brisk pace. N. S. Shenck and J. A. Paradiso [8] at the MIT Media Lab then demonstrated a shoe-mounted device to scavenge electricity from the forces exerted on a shoe during walking. Further researches on improvement in the structures and circuits for the shoe-mounted devices were published at [17-19].

Figure 2. Piezoelectric-powered RFID shoes with mounted electronics.

To realize the power supplement of wireless sensor net work, S. Roundy and P. K. Wright [15] demonstrated a vibration based piezoelectric generator. The device is a piezoelectric bimorph cantilever beam type with proof mass to adjust the resonance frequency. An optimized design demonstrated a power output of 375μW from a vibration source of 2.5m/s^2 at 120Hz. It could be used to power a custom designed 1.9 GHz radio transmitter from the same vibration source. [3]

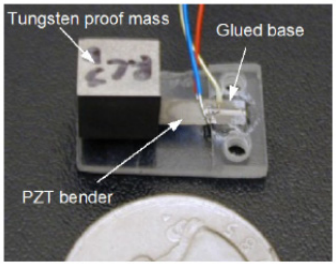

Figure 3. An optimized piezoelectric generator with a 1.5 cm length constraint

Since the mechanical vibration of a piezoelectric element generates an alternating voltage across its electrodes, most of the proposed electrical circuits include an AC–DC converter to provide the electrical energy to its storage device. Guyomar *et al.* [24], Lefeuvre *et al.* [25-27] and Badel *et al.* [28] have developed a new power flow optimization principle based on the extraction of the electric charge produced by a piezoelectric element, synchronized with the mechanical vibration operated at the steady state. They have claimed that the harvested

[3]Similar works based on cantilever beam devices using piezoelectric materials to scavenge vibration energy can be found at [17, 20-23].

electrical power may be increased by as much as 900% over the standard technique. Then, Sue et al. [29] detailed the analysis for the performance of a piezoelectric energy harvesting system using the synchronized switch harvesting on inductor (SSHI) electronic interface. It shows that the electrical response using an ideal SSHI interface is similar to that using the standard interface in a strongly coupled electromechanical system operated at short circuit resonance.

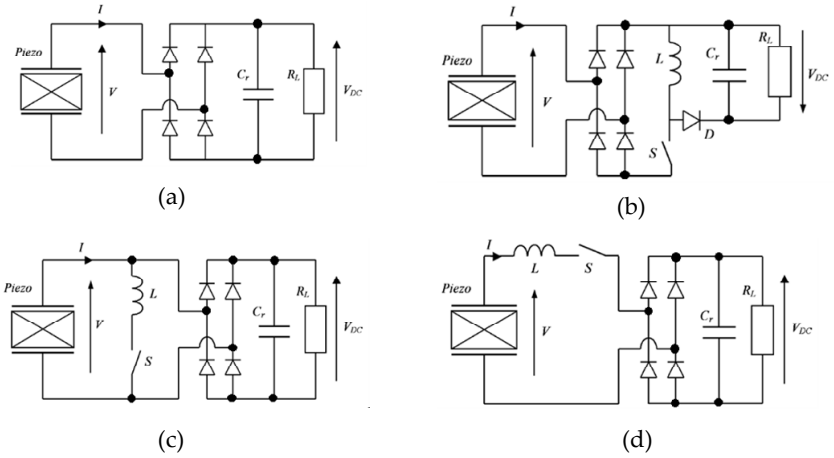

Figure 4. The interface circuits (a) standard interface (b) Synchronous charge extraction (c) Parallel SSHI (d) Series SSHI

For the development of the MEMS devices, Jeon *et al*. [30] have successfully developed the first MEMS based micro-scale power generator using d_{33} mode of PZT material. A 170μm × 260μm PZT beam has been fabricated. A maximum output power of 1.01μW across the load of 5.2MΩ at its resonance frequency of 13.9 kHz has been observed. The corresponding energy density is 0.74mWh/cm^2, which compares favorably to the values of lithium ion batteries.

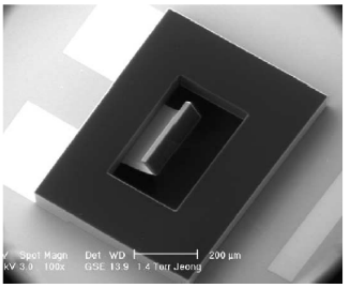

Figure 5. The first MEMS based micro-scale power generator[30]

Fang *et al*. [31, 32] successfully developed a PZT MEMS power-generating device based on the d_{31} mode of piezoelectric transducers that uses top and bottom laminated electrodes. The

cantilever size is of 12μm thick silicon layer, 2000μm × 500μm cantilever in length and width 500μm × 500μm metal mass (length × height), which generated 1.15μW of effective power when connected to a 20.4kΩ resistance load, leading to a 432mV ac voltage. An improved device was announced later that under the 608Hz resonant frequency, the device generated about 0.89V AC peak–peak voltage output to overcome germanium diode rectifier toward energy storage. The power output obtained was of 2.16μW. Some Other MEMS cantilever piezoelectric power generators examples of different materials and structures can be found in [33] and [34]. Other than single beam structures, Figure 7 [35]shows a MEMS power generator array based on thick-film piezoelectric cantilevers. This device can be tuned to the frequency which expanded the excited frequency bandwidth in ambient low frequency vibration.

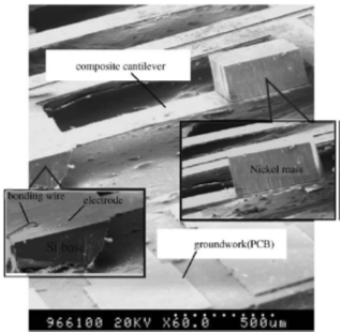

Figure 6. The SEM photo of the fabricated prototype by Fang et al.[32].

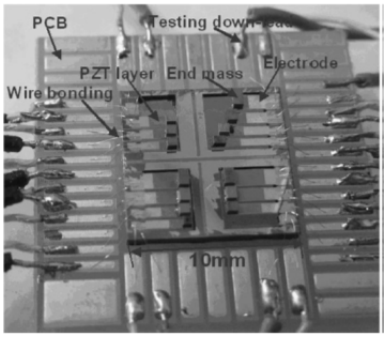

Figure 7. Photograph of power generator array prototype [35]

2. Different types of MEMS power generators and their theoretical models

D_{33} and d_{31} are the two main modes of piezoelectric cantilever beam. In this section, different types of MEMS power generators will be introduced. Readers will be able to see the theoretical models, and the comparison between the experimental results of different

modes. The output performances and characteristics for both the d_{33} mode and the d_{31} mode piezoelectric MEMS generators are evaluated using the same dimensions and with the same materials, with the exception of the differing electrode configuration and dimensions of the proof masses. The two devices were then compared for their resonance frequencies, output powers, output voltages and optimal resistive loads.

2.1. Theoretical model and system equations of d_{31} type

In this section, the theoretical model and the development of a d_{31} mode piezoelectric MEMS generator is presented. The d_{31} mode piezoelectric MEMS generator introduced in this chapter is a cantilever type made by using a silicon process which transforms energy by way of the piezoelectric PZT layer. It is laminated with a PZT layer sandwiched between upper and lower electrodes. The PZT sol-gel process that is suitable for fabricating thin film with a thickness of 1~2μm, is often seen in recent researches. But the PZT deposition processes that is applied in the introduced device uses an own developed PZT deposition machine which adopts a "jet-printing" approach based on an aerosol deposition method. This home-made PZT aerosol machine was developed and constructed in order to fabricate a high-quality PZT thin film more efficiently.

For the modeling and analysis of the output performance of the piezoelectric MEMS generator connected with a resistive load, several methods are available. Electrical equivalent circuit model, force equilibrium analysis and energy method are the commonly used methods [36, 37]. The study of the characteristics of a PZT bender utilizing energy method model has been performed in previous studies and the model has shown fair accuracy in various conditions of mechanical stress. Therefore, the analyzing of the output performance of the device in this chapter will be based on the energy method.

Figure 8 shows the configuration of the d_{31} mode piezoelectric MEMS generator. For fabricating the piezoelectric MEMS generator, a beam structure was manufactured and then covered with a PZT layer with a laminated upper and lower electrode. A proof mass was built at the tip of the beam to adjust the structure resonant frequency of the piezoelectric MEMS generator to fit the most adaptable frequency to match the ambient vibration of the surroundings. The beam structure was designed to operate at resonant frequency for maximum stress and strain so as to also maximize electric power output.

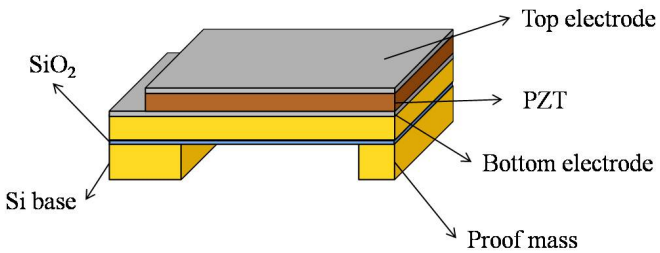

Figure 8. Schematic diagram of the d_{31} mode piezoelectric MEMS generator

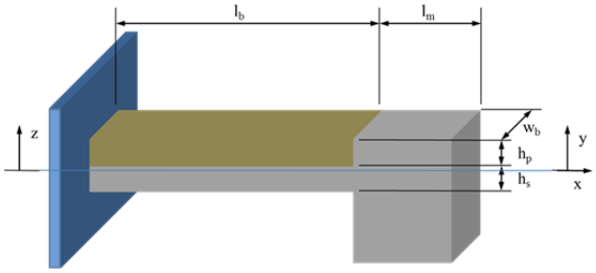

Figure 9. Dimension definitions of the d_{31} mode piezoelectric MEMS generator.

Figure 9 shows the dimension definitions of the d_{31} mode piezoelectric MEMS generator. In the figure, l_b is the length of the beam, l_m the length of the proof mass, h_p the thickness of the piezoelectric material, h_s the thickness of the beam structure (silicon), w_b the width of the beam, z the base vertical displacement and y the distance to the neutral axis of the beam.

The constitutive equations of piezoelectric materials are following the definition in IEEE Standard on Piezoelectric [38]:

$$T_p = c_{pq}^E S_q - e_{kp} E_k \tag{1}$$

$$D_i = e_{iq} S_q + \varepsilon_{ik}^S E_k \tag{2}$$

,where T is the stress (N/m²), S the strain, E the electric field (V/m), D is the electric displacement (Coulomb/m²). "c^E" is the stiffness measured under the constant electric field. "ε^S" is the dielectric constant or permittivity under constant strain. "e" is the piezoelectric constant (Coulomb/m²).

Some other forms of the constitutive equations are:

$$S_q = s_{pq}^E T_p + d_{kq} E_k \tag{3}$$

$$D_i = d_{ip} T_p + \varepsilon_{ik}^T E_k \tag{4}$$

$$S_q = s_{pq}^D T_p + g_{kq} D_k \tag{5}$$

$$E_i = -g_{ip} T_p + \beta_{ik}^T D_k \tag{6}$$

$$T_p = c_{pq}^D S_q - h_{kp} D_k \tag{7}$$

$$E_i = -h_{iq} S_q + \beta_{ik}^S D_k \tag{8}$$

Equation (1) and (2) can be written in a matrix form:

$$\begin{Bmatrix} \mathbf{T} \\ \mathbf{D} \end{Bmatrix} = \begin{bmatrix} \mathbf{c}^{\mathrm{E}} & -\mathbf{e} \\ \mathbf{e} & \boldsymbol{\varepsilon}^{\mathrm{S}} \end{bmatrix} \begin{Bmatrix} \mathbf{S} \\ \mathbf{E} \end{Bmatrix} \tag{9}$$

The model for a d_{31} type cantilever beam with piezoelectric elements MEMS generator can be obtained with an energy method approach. The generalized form of Hamilton's Principle for an electromechanical system, neglecting the magnetic terms and defining the kinetic (T_k), internal potential (U), and electrical (W_e) energies, as well as the external work (W), is given by:

$$V.I. = \int_{t_1}^{t_2} [\delta(T_k - U + W_e) + \delta W] dt = 0 \tag{10}$$

The individual energy terms are defined as:

$$T_k = \int_{V_s} \frac{1}{2} \rho_s \dot{\mathbf{u}}^t \dot{\mathbf{u}} dV_s + \int_{V_p} \frac{1}{2} \rho_p \dot{\mathbf{u}}^t \dot{\mathbf{u}} dV_p \tag{11}$$

$$U = \int_{V_s} \frac{1}{2} \mathbf{S}^t \mathbf{T} dV_s + \int_{V_p} \frac{1}{2} \mathbf{S}^t \mathbf{T} dV_p \tag{12}$$

$$W_e = \int_{V_p} \frac{1}{2} \mathbf{E}^t \mathbf{D} dV_p + \int_{V_{pe}} \frac{1}{2} \mathbf{E}^t \mathbf{D} dV_{pe} \tag{13}$$

The subscripts *s*, *p* and *pe* indicate the inactive (structural) sections of the beam volume, the piezoelectric element of the beam volume and the piezoelectric element outside the beam structure respectively. The mechanical displacement is denoted by $u(x,t)$ with ρ the density. The contributions to *We* due to fringing fields in the structure and free space are neglected.

Considering *nf* discretely applied external point forces, $f_k(t)$, at positions x_k , and *nq* charges, q_j, applied at discrete electrodes with positions x_j , the external work term is defined in terms of the local mechanical displacement, $u_k = u(x_k, t)$, and the scalar electrical potential, $\phi_j = \phi(\mathbf{x_j}, t)$:

$$\delta W = \sum_{k=1}^{nf} \delta \mathbf{u}_k \mathbf{f}_k(t) - \sum_{j=1}^{nq} \delta \phi_j q_j(t) \tag{14}$$

The above definitions, as well as the constitutive relations of a piezoelectric material (1-9), are used in conjunction with a variational approach to rewrite equation (10):

$$\int_{t_1}^{t_2} \left[\begin{array}{l} \int_{V_s} \rho_s \delta \dot{\mathbf{u}}^t \dot{\mathbf{u}} dV_s + \int_{V_p} \rho_p \delta \dot{\mathbf{u}}^t \dot{\mathbf{u}} dV_p - \int_{V_s} \delta \mathbf{S}^t \mathbf{c}_s \mathbf{S} dV_s - \int_{V_p} \delta \mathbf{S}^t \mathbf{c}^{\mathrm{E}} \mathbf{S} dV_p \\ + \int_{V_p} \delta \mathbf{S}^t \mathbf{e}^t \mathbf{E} dV_p + \int_{V_p} \delta \mathbf{E}^t \mathbf{e} \mathbf{S} dV_p + \int_{V_p} \delta \mathbf{E}^t \varepsilon^S \mathbf{E} dV_p \\ + \int_{V_{pe}} \delta \mathbf{E}^t \varepsilon^S \mathbf{E} dV_{pe} + \sum_{k=1}^{nf} \delta \mathbf{u}_k \mathbf{f}_k(t) - \sum_{j=1}^{nq} \delta \phi_j q_j(t) \end{array} \right] dt = 0 \tag{15}$$

Three basic assumptions are introduced: the Rayleigh-Ritz procedure, Euler-Bernoulli beam theory, and that the electrical field across the piezoelectric is constant. In the Rayleigh-Ritz approach, the displacement of a structure can be written as the sum of *nr* individual modes, $\psi_{ri}(x)$, multiplied by a mechanical temporal coordinate, $r_i(t)$. For a beam in bending status, only the transverse displacement is considered and the mode shape is a function only of the axial position, x. Furthermore, the base excitation is assumed to be in the transverse direction as well:

$$\mathbf{u}(\mathbf{x},t) = \sum_{i=1}^{nr} \psi_{ri}(x) r_i(t) = \psi_r(x)\mathbf{r}(t) \tag{16}$$

Similarly, the electric potential for each of the *nq* electrode pairs can be written in terms of a potential distribution, ψ_{vj} , and the electrical temporal coordinate, $v_j(t)$.

$$\phi(\mathbf{x},t) = \sum_{j=1}^{nq} \psi_{vj}(\mathbf{x}) v_j(t) = \psi_v(\mathbf{x})\mathbf{v}(t) \tag{17}$$

The Euler-Bernoulli beam theory allows the axial strain in the beam to be written in terms of the beam displacement and the distance from the neutral axis as:

$$\mathbf{S}(\mathbf{x},t) = -y\frac{\partial^2 u(x,t)}{\partial x^2} = -y\psi_r{}''\mathbf{r}(t) \tag{18}$$

Because the MEMS power generator is a composite beam structure, the actual composite beam can be replaced with an equivalent beam made of one material to simplify the analysis. Therefore, the silicon material will be represented by the piezoelectric material in the following derivation. For the composite beam structure, the neutral axis is located at $\bar{y}$ (from the bottom of the beam):

$$\bar{y} = \frac{2c_p h_p h_s + c_p h_p^2 + c_s h_s^2}{2\left(c_p h_p + c_s h_s\right)} \tag{19}$$

, where c_p and c_s are the stiffness of the piezoelectric material and the silicon. Noted that for a special case which the neutral axis is right at the interface of the piezoelectric material and the silicon, the thickness of the piezoelectric material can be obtained from equation (19):

$$h_p = \sqrt{\frac{c_s}{c_p}} h_s \tag{20}$$

The bending rigidity of the composite beam structure could be shown as:

$$\frac{w_b\left(c_p^2 h_p^4 + 4c_p h_p^3 c_s h_s + 6c_p h_p^2 c_s h_s^2 + 4c_p h_p c_s h_s^3 + c_s^2 h_s^4\right)}{12\left(c_p h_p + c_s h_s\right)} \tag{21}$$

In order for replacing the silicon material by the piezoelectric material, the ratio of the elastic constant of the silicon to piezoelectric material, $\eta_s=c_s/c_p$, is used. Then the effective moment of inertia can be obtained from equation (21):

$$\begin{aligned} \mathrm{I} &= \frac{w_b\left(h_p^4+4h_p^3h_s\eta_s+6h_p^2h_s^2\eta_s+4h_ph_s^3\eta_s+h_s^4\eta_s^2\right)}{12\left(h_p+h_s\eta_s\right)} \\ &= \frac{\left(\mu_h^4+4\mu_h\eta_s+6\mu_h^2\eta_s+4\mu_h^3\eta_s+\eta_s^2\right)}{12\left(\mu_h+\eta_s\right)}w_bh_s^3 \end{aligned} \tag{22}$$

, where $\mu_h = h_p/h_s$. If the neutral axis is right at the interface of the piezoelectric material and the silicon, the effective moment of inertia can be simplified from equation (22):

$$\mathrm{I} = \frac{w_bh_p^2\left(h_p+h_s\right)}{3} \tag{23}$$

Substituting Equations (16), (17) and (18) into Equation (15), the above equation can be written in terms of mass, M, stiffness, K, coupling, Θ, and capacitive terms, C_p, to obtain the governing equations in Equations bellow:

$$\mathbf{M}\ddot{\mathbf{r}}+\mathbf{K}\mathbf{r}-\mathbf{\Theta}\mathbf{v}=\sum_{k=1}^{nf}\psi_r^t(x_k)\cdot f_k(t) \tag{24}$$

$$\mathbf{\Theta}^t\mathbf{r}+\mathbf{C_p}\mathbf{v}=\sum_{j=1}^{nq}\psi_v(\mathbf{x}_j)\cdot q_j(t) \tag{25}$$

where,

$$\mathbf{M}=\int_{V_s}\psi_r^t\rho_s\psi_r dV_s+\int_{V_p}\psi_r^t\rho_p\psi_r dV_p \tag{26}$$

$$\mathbf{K}=\int_{V_s}(-y\psi_r'')^t\mathbf{c}_s(-y\psi_r'')dV_s+\int_{V_p}(-y\psi_r'')^t\mathbf{c}^E(-y\psi_r'')dV_p \tag{27}$$

$$\mathbf{\Theta}=\int_{V_p}(-y\psi_r'')^t\mathbf{e}^t(-\nabla\cdot\psi_v)dV_p \tag{28}$$

$$\mathbf{C_p}=\int_{V_p}(-\nabla\cdot\psi_v)^t\varepsilon^S(-\nabla\cdot\psi_v)dV_p+\int_{V_{pe}}(-\nabla\cdot\psi_v)^t\varepsilon^S(-\nabla\cdot\psi_v)dV_{pe} \tag{29}$$

The applied external force input to the system is the base excitation is denoted as $\ddot{z}_B$. The loading is summated for all the elements and can be reduced to the integral over the structure length. Assumed that the device is uniform in the axial direction, the right hand side of equation (24) can be written as:

$$\int\psi_r^t(x)\cdot f(t)=\int_0^{l_b}\psi_r^t(x)\cdot(-m\ddot{z}_B)dx=\mathbf{F}_\mathrm{B}\ddot{z}_B \tag{30}$$

, where $\mathbf{F_B}$ is the forcing vector for the uniform device in the axial direction. However, the device now consists of two separate sections, the uniform beam and uniform proof mass. Both contribute to the inertial loading of the device. The proof mass displacement is calculated in terms of the displacement and rotation of the tip of the beam. A forcing function is defined in terms of the mass per length of the proof mass, mm, and two additional terms are calculated to make up the modified input matrix [39]:

$$\mathbf{F}_{\mathrm{B}} = -\left(m\int_0^{l_b} \psi_r^t(x)dx + m_m\int_{l_b}^{l_b+l_m} \psi_r^t(l_b)dx + m_m\int_{l_b}^{l_b+l_m} \left(\psi_r'(l_b)x\right)^t dx \right) \tag{31}$$

Mechanical damping can be added through the addition of a damping matrix, *C*, to equation (24). The right hand side term of equation (25) can be differentiated with respect to time to obtain current. The current can be related to the voltage, assuming that the electrical loading is a resistor, R_l.

$$\mathbf{M}\ddot{\mathbf{r}} + \mathbf{C}\dot{\mathbf{r}} + \mathbf{K}\mathbf{r} - \boldsymbol{\Theta}\mathbf{v} = \mathbf{F}_{\mathbf{B}}\ddot{z}_B \tag{32}$$

$$\boldsymbol{\Theta}^t\dot{\mathbf{r}} + \mathbf{C}_{\mathbf{p}}\dot{\mathbf{v}} + \frac{1}{R_l}\mathbf{v} = 0 \tag{33}$$

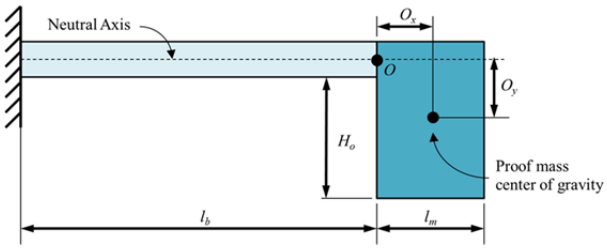

Figure 10. Schematic diagram of the assumed beam configuration

In order to lower the resonance frequency of the piezoelectric energy harvester, it needs to add a proof mass at the tip of the cantilever beam. Figure 10 is the schematic diagram of the beam with tip proof mass. It is assumed that the center of gravity of the mass does not coincide with the end of the beam, *O*. The Euler-Bernoulli beam theory is used to determine the governing equations in terms of the mechanical displacement:

$$EI\,\psi_{rN}^{(4)} - m\omega^2\psi_{rN} = 0 \tag{34}$$

and can be solved generally for the N$^{\text{th}}$ mode:

$$\psi_{rN} = c\sinh\lambda_N x + d\cosh\lambda_N x + e\sin\lambda_N x + f\cos\lambda_N x \tag{35}$$

The constants (*c*, *d*, *e*, and *f*) can be solved by using the boundary conditions of the beam with the mass. With a reasonable assumption that the both the beam and the proof mass are uniform in the axial direction with mass per lengths of m and mm, respectively, it is possible

to determine the boundary conditions at the point where the beam and the mass are connected, y_{lb}:

$$EIy''_{lb} - \omega_N^2 I_0 y'_{lb} - \omega_N^2 S_0 y_{lb} = 0 \tag{36}$$

$$EIy'''_{lb} + \omega_N^2 M_0 y_{lb} + \omega_N^2 S_0 y'_{lb} = 0 \tag{37}$$

where: $M_0 = m_m l_m$, $S_0 = M_0 O_x$, $I_0 = I_{yy} + M_0(O_x^2 + O_y^2)$, E is the axial modulus of the beam, I is the second moment of area of the beam, I_{yy} is the moment of inertia of the proof mass around its center of gravity, and ω_N is the natural frequency of the beam. By defining $\bar{\lambda}_N = \lambda_N l_b$, $\bar{M}_0 = M_0 O_x$, $\bar{S}_0 = S_0 / m l_b^2$ and $\bar{I}_0 = I_0 / m l_b^3$, the boundary conditions are used to obtain the matrix equation.

$$\begin{bmatrix} A_{11} & A_{12} \\ A_{21} & A_{22} \end{bmatrix} \begin{bmatrix} e \\ f \end{bmatrix} = 0 \tag{38}$$

$$\begin{aligned} A_{11} = {} & \left(\sinh\bar{\lambda}_N + \sin\bar{\lambda}_N\right) + \bar{\lambda}_N{}^3 \bar{I}_0 \left(-\cosh\bar{\lambda}_N + \cos\bar{\lambda}_N\right) \\ & + \bar{\lambda}_N{}^2 \bar{S}_0 \left(-\sinh\bar{\lambda}_N + \sin\bar{\lambda}_N\right) \end{aligned} \tag{39}$$

$$\begin{aligned} A_{12} = {} & \left(\cosh\bar{\lambda}_N + \cos\bar{\lambda}_N\right) + \bar{\lambda}_N{}^3 \bar{I}_0 \left(-\sinh\bar{\lambda}_N - \sin\bar{\lambda}_N\right) \\ & + \bar{\lambda}_N{}^2 \bar{S}_0 \left(-\cosh\bar{\lambda}_N + \cos\bar{\lambda}_N\right) \end{aligned} \tag{40}$$

$$\begin{aligned} A_{21} = {} & \left(\cosh\bar{\lambda}_N + \cos\bar{\lambda}_N\right) + \bar{\lambda}_N \bar{M}_0 \left(\sinh\bar{\lambda}_N - \sin\bar{\lambda}_N\right) \\ & + \bar{\lambda}_N{}^2 \bar{S}_0 \left(\cosh\bar{\lambda}_N - \cos\bar{\lambda}_N\right) \end{aligned} \tag{41}$$

$$\begin{aligned} A_{22} = {} & \left(\sinh\bar{\lambda}_N - \sin\bar{\lambda}_N\right) + \bar{\lambda}_N \bar{M}_0 \left(\cosh\bar{\lambda}_N - \cos\bar{\lambda}_N\right) \\ & + \bar{\lambda}_N{}^2 \bar{S}_0 \left(\sinh\bar{\lambda}_N + \sin\bar{\lambda}_N\right) \end{aligned} \tag{42}$$

The mode resonance frequencies can be obtained by solving for $\bar{\lambda}_N$ such that $\begin{vmatrix} A_{11} & A_{12} \\ A_{21} & A_{22} \end{vmatrix} = 0$. Successive values of $\bar{\lambda}_N$ correspond to the modes of the beam and the natural frequency of each mode can be determined with: $\omega_N^2 = \bar{\lambda}_N^2 \sqrt{\dfrac{EI}{m l_b^4}}$. The solution of equation (35) can be written in terms of a single arbitrary constant, say f:

$$\psi_{rN} = f\left[\left(\cosh\lambda_N x - \cos\lambda_N x\right) - A_{12} / A_{11}\left(\sinh\lambda_N x - \sin\lambda_N x\right)\right] \tag{43}$$

The effective mass of the structure can be obtained from the Lagrange equations of motion and replaces equation (26) when a proof mass is added to a cantilever beam.

$$\begin{aligned}\mathbf{M} = &\int_{V_s} \psi_r^t \rho_s \psi_r dV_s + \int_{V_p} \psi_r^t \rho_p \psi_r dV_p + M_0 \psi_r^t(l_b)\psi_r(l_b) \\ &+ 2S_0 M_0 \psi_r^t(l_b)\psi_r'(l_b) + I_0 M_0 \psi_r^t(l_b)\psi_r'(l_b)\end{aligned} \tag{44}$$

The governing equation shown in (32) can be written in an alternative form by dividing through by **M** and making use of the definitions $\omega_1 = \sqrt{K/M}$ and $\zeta_m = C/2M\omega_1$:

$$\ddot{r} + 2\zeta_m \omega_1 \dot{r} + \omega_1^2 r - \Theta/M\, v = F_B \ddot{z}_B / M \tag{45}$$

$$\Theta \dot{r} + C_p \dot{v} + \frac{1}{R_l} v = 0 \tag{46}$$

The dimensionless factors $\tau = \omega_1 R_l C_p$, $\kappa^2 = \Theta^2 / KC_p$ and $\Omega = \omega/\omega_1$ are introduced, where ω is the base input frequency and the system response is calculated:

$$\left|\frac{r}{F_B \ddot{z}_B}\right| = \frac{1}{K} \frac{\sqrt{1+(\tau\Omega)^2}}{\sqrt{\left[1-\left(1+2\zeta_m\tau\right)\Omega^2\right]^2 + \left[\left(2\zeta_m + \left(1+\kappa^2\right)\tau\right)\Omega - \tau\Omega^3\right]^2}} \tag{47}$$

$$\left|\frac{v}{F_B \ddot{z}_B}\right| = \frac{1}{\Theta} \frac{\kappa^2 \tau\Omega}{\sqrt{\left[1-\left(1+2\zeta_m\tau\right)\Omega^2\right]^2 + \left[\left(2\zeta_m + \left(1+\kappa^2\right)\tau\right)\Omega - \tau\Omega^3\right]^2}} \tag{48}$$

$$\left|\frac{P}{\left(F_B \ddot{z}_B\right)^2}\right| = \frac{1}{2\sqrt{MK}} \frac{\kappa^2 \tau\Omega^2}{\left[1-\left(1+2\zeta_m\tau\right)\Omega^2\right]^2 + \left[\left(2\zeta_m + \left(1+\kappa^2\right)\tau\right)\Omega - \tau\Omega^3\right]^2} \tag{49}$$

Equation (47) gives the generalized mechanical displacement, which can be converted to actual displacements by multiplying it with the mode shape. The system can be analyzed at short-circuit and open-circuit conditions by letting the electrical load resistance tending to zero and infinity, respectively. Two optimal frequency ratios for maximum power generation can be obtained, which correspond to the resonance (subscript sc) and anti-resonance (subscript oc) frequencies of the beam structure:

$$\Omega_{sc} = 1, \qquad \Omega_{oc} = \sqrt{1+\kappa^2} \tag{50}$$

The power can be optimized with respect to the load resistance to obtain an optimal electrical load. This is achieved by optimizing the power with respect to the dimensionless constant, τ:

$$\tau_{opt} = \frac{1}{\Omega} \sqrt{\frac{\left(\Omega^2 - 1\right)^2 + \left(2\Omega\zeta_m\right)^2}{\left(\Omega^2 - (\kappa^2 + 1)\right)^2 + \left(2\Omega\zeta_m\right)^2}} \tag{51}$$

Substituting equation (51) into power equation (49) can found that:

$$\left|\frac{P}{\left(F_B\ddot{z}_B\right)^2/2\sqrt{MK}}\right| = \frac{\frac{\Omega}{\kappa^2}\sqrt{\left(\frac{\Omega^2-1}{2\kappa^2\Omega}\right)^2+\left(\frac{\zeta_m}{\kappa^2}\right)^2}}{\left(8\left(\frac{\zeta_m}{\kappa^2}\right)^2\Omega^2+2\left(\frac{\Omega^2-1}{\kappa^2}\right)^2\right)\sqrt{\left(\frac{\Omega^2-\left(1+\kappa^2\right)}{2\kappa^2\Omega}\right)^2+\left(\frac{\zeta_m}{\kappa}\right)^2}+4\left(\frac{\zeta_m}{\kappa^2}\right)\Omega\sqrt{\left(\frac{\Omega^2-1}{2\kappa^2\Omega}\right)^2+\left(\frac{\zeta_m}{\kappa^2}\right)^2}} \quad (52)$$

It can be found that except the geometric dimensions, the output power is only the function of Ω, ζm and κ. For MEMS-scale devices, ζ_m is generally at least an order of magnitude smaller than κ^2 [40]. With this assumption, the power output at both the resonance and anti-resonance frequencies (under optimal electrical load) is approximated as:

$$\left|P_{opt}\right| \approx \frac{\left(F_B\ddot{z}_B\right)^2}{16\sqrt{MK}\zeta_m} \quad (53)$$

2.2. Theoretical model and system equations of d_{33} type

This section presents the theoretical model and the development of the d_{33} mode piezoelectric MEMS generator. It is composed of interdigitated electrodes at the top of the PZT layer. The aerosol deposition method is also adopted to fabricate a high-quality PZT thin film more efficiently.

For piezoelectric elements, the longitudinal piezoelectric effect can be much larger than the traverse effect ($d_{33}/d_{31} \sim 2.4$ for most piezoelectric ceramics [41]). For this reason, it is desirable to operate the device in the d_{33} mode. The d_{33} mode operation occurs when the electric field and the strain direction coincide. Figure 11 shows the configuration of the d_{33} mode piezoelectric MEMS generator. For fabricating the piezoelectric MEMS generator, a beam structure was manufactured and then covered with a PZT layer with a laminated upper electrode. A proof mass was also built at the tip of the beam.

Since the output voltage is a function of the output charge and the capacitance between the interdigitated electrodes, the output voltage can be adjusted by the distance between the interdigitated electrodes. Therefore, the following text will also show readers the relationships between the distance of the interdigitated electrodes with the output voltage and power output performance.

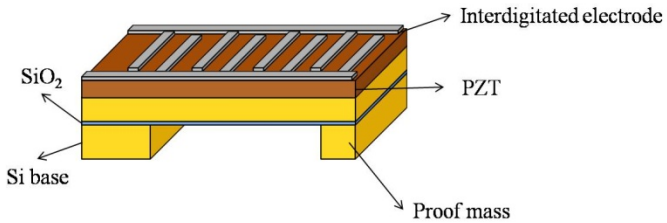

Figure 11. Schematic diagram of the d_{33} mode piezoelectric MEMS generator

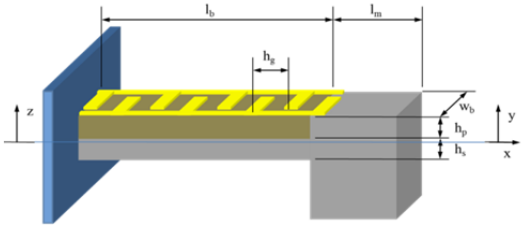

Figure 12. Dimension definitions of the d33 mode piezoelectric MEMS generator.

Figure 12 shows the dimension definitions of the d33 mode piezoelectric MEMS generator. In the figure, l_b is the length of the beam, l_m the length of the proof mass, h_p the thickness of the piezoelectric material, h_s the thickness of the beam structure (silicon), h_g the interval of the interdigitated electrodes, w_b the width the beam, z the base vertical displacement and y the distance to the neutral axis the beam.

Since the electric field is not completely in the axial direction through the thickness of the piezoelectric element, nor is the section of piezoelectric element under the electrode completely inactive, an approximate model for the interdigitated electrode-configuration has been adopted. It is assumed that the region of the piezoelectric element under the electrode is electrically inactive, whereas the section between the electrodes utilizes the full d33 effect. Figure 13 shows the geometry of the approximate model.

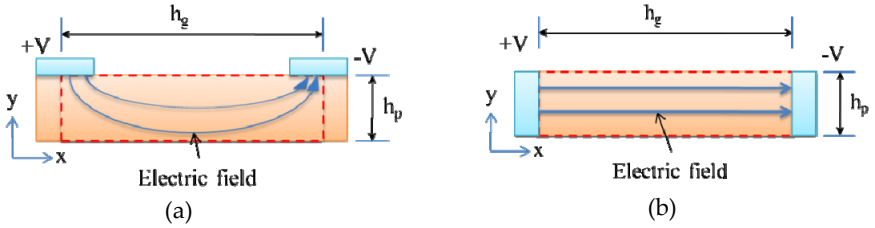

Figure 13. (a) Interdigitated electrode configuration (b) the model approximation

The model for a d33 type cantilever beam with piezoelectric elements MEMS generator can be obtained with an energy method approach. The generalized form of Hamilton's Principle for modeling the electromechanical system is as shown in equation (10). The individual energy terms (the kinetic T_k, internal potential U, and electrical W_e) are defined in equations (11), (12), and (13). It is important to note that although the device is made up of a number of separate piezoelectric regions, there is only one electrode pair and the voltage across all the elements will be the same. Since the strain varies along the length of the beam, different amounts of charge will be generated in each region and the charge sums to give the total charge output of the device. Therefore, the electric potential can be written as:

$$\phi(\mathbf{x},t) = \psi_v(\mathbf{x})\bar{\mathbf{v}}(t) \tag{54}$$

Following the procedure and the assumptions in the previous section and considering only one interdigitated electrode pairs, the governing equations can be rewritten as:

$$\mathbf{M}\ddot{\mathbf{r}} + \mathbf{C}\dot{\mathbf{r}} + \mathbf{K}\mathbf{r} - \boldsymbol{\Theta}\overline{\mathbf{v}} = \mathbf{F}_{\mathbf{B}}\ddot{z}_B \tag{55}$$

$$\boldsymbol{\Theta}^t\dot{\mathbf{r}} + \mathbf{C}_{\mathbf{p}}\dot{\overline{\mathbf{v}}} + \frac{1}{R_l}\overline{\mathbf{v}} = 0 \tag{56}$$

where,

$$\begin{aligned}\mathbf{M} = &\int_{V_s}\psi_r^t\rho_s\psi_r dV_s + \int_{V_p}\psi_r^t\rho_p\psi_r dV_p + M_0\psi_r^t(l_b)\psi_r(l_b)\\ &+ 2S_0M_0\psi_r^t(l_b)\psi_r'(l_b) + I_0M_0\psi_r'^t(l_b)\psi_r'(l_b)\end{aligned} \tag{57}$$

$$\mathbf{K} = \int_{V_s}(-y\psi_r'')^t\mathbf{c}_s(-y\psi_r'')dV_s + \int_{V_p}(-y\psi_r'')^t\mathbf{c}^E(-y\psi_r'')dV_p \tag{58}$$

$$\boldsymbol{\Theta} = \int_{V_p}(-y\psi_r'')^t\mathbf{e}^t(-\nabla\cdot\psi_v)dV_p \tag{59}$$

$$\mathbf{C}_{\mathbf{p}} = \int_{V_p}(-\nabla\cdot\psi_v)^t\varepsilon^S(-\nabla\cdot\psi_v)dV_p \tag{60}$$

$$\mathbf{F}_{\mathrm{B}} = -\left(m\int_0^{l_b}\psi_r^t(x)dx + m_m\int_{l_b}^{l_b+l_m}\psi_r^t(l_b)dx + m_m\int_{l_b}^{l_b+l_m}\left(\psi_r'(l_b)x\right)^t dx\right) \tag{61}$$

In order to lower the resonance frequency of the piezoelectric energy harvester, a proof mass was added at the tip of the cantilever beam. The modal shape for a cantilever beam with the addition of the mass is shown as in equation (34). The following electric potential distribution is assumed to give a constant electric field in one piezoelectric element between interdigitated electrode pair. The potential distribution varies from +1 at the electrode on one side to 0 at the electrode on the other side. The function ψ_v can be shown as:

$$\begin{aligned}&\psi_v = \begin{cases} x/h_g, & 2kh_g \le x \le (2k+1)h_g \\ -x/h_g + 2, & (2k+1)h_g \le x \le 2(k+1)h_g \end{cases}\\ &k = 0,1,2\ldots\end{aligned} \tag{62}$$

The governing equation shown in (55) and (56) can be written in an alternative form by dividing through by M and making use of the definitions $\omega_1 = \sqrt{K/M}$ and $\zeta_m = C/2M\omega_1$:

$$\ddot{r} + 2\zeta_m\omega_1\dot{r} + \omega_1^2 r - \Theta/M\,\overline{v} = F_B\ddot{z}_B/M \tag{63}$$

$$\Theta\dot{r} + C_p\dot{\overline{v}} + \frac{1}{R_l}\overline{v} = 0 \tag{64}$$

The dimensionless factors $\tau = \omega_1 R_l C_p$, $\kappa^2 = \Theta^2/KC_p$ and $\Omega = \omega/\omega_1$ are introduced, where ω is the base input frequency and the system response is calculated:

$$\left|\frac{r}{F_B\ddot{z}_B}\right| = \frac{1}{K}\frac{\sqrt{1+\left(\tau\Omega\right)^2}}{\sqrt{\left[1-\left(1+2\zeta_m\tau\right)\Omega^2\right]^2+\left[\left(2\zeta_m+\left(1+\kappa^2\right)\tau\right)\Omega-\tau\Omega^3\right]^2}} \tag{65}$$

$$\left|\frac{\overline{v}}{F_B\ddot{z}_B}\right| = \frac{1}{\Theta}\frac{\kappa^2\tau\Omega}{\sqrt{\left[1-\left(1+2\zeta_m\tau\right)\Omega^2\right]^2+\left[\left(2\zeta_m+\left(1+\kappa^2\right)\tau\right)\Omega-\tau\Omega^3\right]^2}} \tag{66}$$

$$\left|\frac{P}{\left(F_B\ddot{z}_B\right)^2}\right| = \frac{1}{2\sqrt{MK}}\frac{\kappa^2\tau\Omega^2}{\left[1-\left(1+2\zeta_m\tau\right)\Omega^2\right]^2+\left[\left(2\zeta_m+\left(1+\kappa^2\right)\tau\right)\Omega-\tau\Omega^3\right]^2} \tag{67}$$

The results are identical to the d_{31} mode piezoelectric MEMS generator as shown in (47), (48), and (49).

The system can be analyzed at short-circuit and open-circuit conditions by letting the electrical load resistance tending to zero and infinity, respectively. Two optimal frequency ratios for maximum power generation can be obtained, which correspond to the resonance and anti-resonance frequencies of the beam structure:

$$\Omega_{sc} = 1, \qquad \Omega_{oc} = \sqrt{1+\kappa^2} \tag{68}$$

The power can be optimized with respect to the load resistance to obtain an optimal electrical load. This is achieved by optimizing the power with respect to the dimensionless constant, τ:

$$\tau_{opt} = \frac{1}{\Omega}\sqrt{\frac{\left(\Omega^2-1\right)^2+\left(2\Omega\zeta_m\right)^2}{\left(\Omega^2-\left(\kappa^2+1\right)\right)^2+\left(2\Omega\zeta_m\right)^2}} \tag{69}$$

This is the same as the results of the d_{31} mode piezoelectric MEMS generator as shown in (51). Substituting equation (69) into power equation (67) can found that:

$$\left|\frac{\mathrm{P}}{\left(F_B\ddot{z}_B\right)^2/2\sqrt{MK}}\right| = \frac{\frac{\Omega}{\kappa^2}\sqrt{\left(\frac{\Omega^2-1}{2\kappa^2\Omega}\right)^2+\left(\frac{\zeta_m}{\kappa^2}\right)^2}}{\left(8\left(\frac{\zeta_m}{\kappa^2}\right)^2\Omega^2+2\left(\frac{\Omega^2-1}{\kappa^2}\right)^2\right)\sqrt{\left(\frac{\Omega^2-\left(1+\kappa^2\right)}{2\kappa^2\Omega}\right)^2+\left(\frac{\zeta_m}{\kappa}\right)^2}+4\left(\frac{\zeta_m}{\kappa^2}\right)\Omega\sqrt{\left(\frac{\Omega^2-1}{2\kappa^2\Omega}\right)^2+\left(\frac{\zeta_m}{\kappa^2}\right)^2}} \tag{70}$$

It can be found that except the geometric dimensions, the output power is only the function of Ω, ζ_m and κ. With the assumption that for MEMS-scale devices, ζ_m is generally at least an order of magnitude smaller than κ^2 [40], the power output at both the resonance and anti-resonance frequencies (under optimal electrical load) is approximated as:

$$\left|P_{opt}\right| \approx \frac{\left(F_B \ddot{z}_B\right)^2}{16\sqrt{MK}\zeta_m} \tag{71}$$

3. Fabrication of piezoelectric MEMS power generators

3.1. PZT deposition method

Fabricating the PZT layer using an aerosol deposition method has been proven to be a quick, efficient and easy-to-pattern MEMS process [42, 43]. The aerosol deposition equipment deposited PZT film up to 0.1 micrometer per minute. Figure 14 shows the schematic diagram of the aerosol deposition equipment. The PZT powder with a particle size smaller than 1μm in diameter was put in a continuously vibrating powder chamber in order to suspend the PZT particles. Nitrogen or Helium gas was connected to the powder chamber with gas flow rate of 4~6 liters per minute so as to bring the PZT particles through the nozzle and into the deposition chamber. With the deposition chamber in a vacuum, the pressure difference between the power chamber and the deposition chamber accelerated the PZT particles and forced them to jet out from the nozzle inside the deposition chamber and deposit onto the wafer surface with high speed. The wafer substrate was then carried by an X-Y moving stage so that deposition over the entire area of the PZT took place. Both the flow rate of the inlet gas and the scan speed of the X-Y moving stage were then used to control the deposition rate and the roughness of the deposited PZT layer.

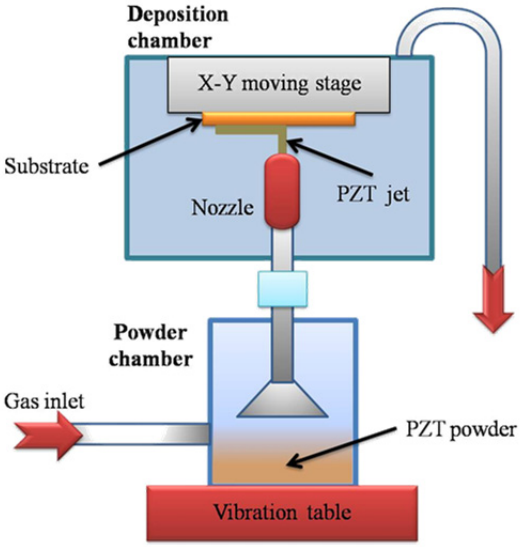

Figure 14. Schematic diagram of the aerosol deposition machine

Figure 15 shows the SEM photography of the PZT layer as deposited by aerosol deposition with a thickness of up to 28μm. A lift-off method was adopted to pattern the PZT layer that

was deposited by the aerosol deposition machine. A photoresist[4] with suitable hardness and adhesion between the photoresist and PZT powder was needed for the lift-off process to prevent damage to the photoresist during processing and to limit accumulation of the PZT powder at the sidewall. Figure 16 shows the SEM photograph of the sidewall of the PZT layer patterned by the lift-off method.

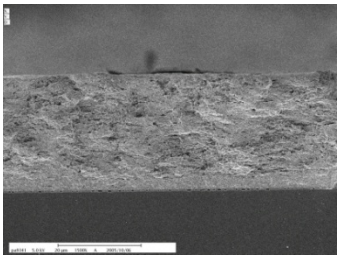

Figure 15. SEM Photograph of the cross-sectional view of 28μm thickness PZT layer after deposition

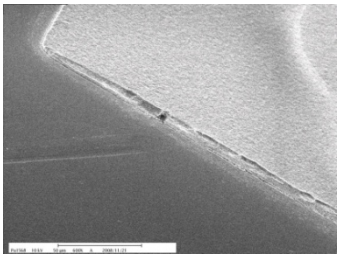

Figure 16. SEM Photograph of a patterned PZT layer by lift-off method

An annealing process was required to improve the characteristics of the material. To investigate the effects at different annealing temperatures, the relationship between polarization and the electric field of the annealed PZT film with 5μm in thickness at different annealing temperatures were undertaken using a ferroelectric analyzer (TF ANALYZER 2000). Figure 17 shows the measured P-E hysteresis curves. The applied electrical field was 75MV/m at 100Hz. The remnant polarizations were 7~9.3μC/cm2 after annealing above 450°C, which shows much improvement when compared to non-annealed PZT layers. The measurement results show that the coercive field decreased with respect to an increase in annealing temperature.

The crystalline phase of the deposited PZT layer associated with the different annealed temperatures can be characterized by XRD (x-ray diffraction). The non-annealed crystalline phase was used as a reference point. (See figure 18) The findings indicate that a perovskite phase in the PZT powder remains after a 650°C annealing process. Therefore, after the PZT film was deposited, it was then annealed at 650°C for 3 hours in a furnace and then cooled to room temperature. It should be noticed that PZT microstructures will crack easily when

[4] A photoresist KMPR-1050 (MicroChem Corp.) or THB-151N (JSR Micro Inc.) was used in this work.

the annealing temperature is higher than 700°C. Similarly, acceptable piezoelectric constants cannot be obtained for annealing temperature lower than 450°C.

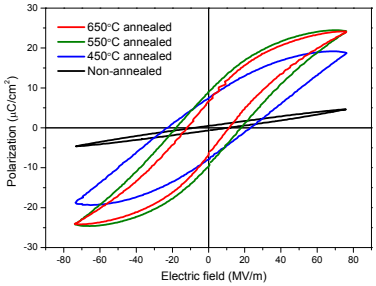

Figure 17. P-E hysteresis curve of a 5μm PZT layer at different annealing temperatures

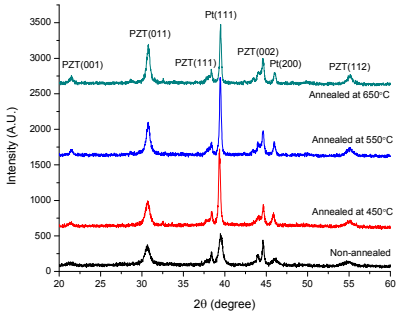

Figure 18. XRD scan of the PZT layers at different annealing temperatures

3.2. MEMS fabrication process of the device

The piezoelectric MEMS generator was a laminated cantilever structure which was composed of a supporting silicon membrane, a piezoelectric layer and laminated electrodes. Both the d_{31} and d_{33} mode piezoelectric MEMS generator introduced in this chapter were designed to incorporate a 3000×1500μm^2 size cantilever beam structure with an 11μm thickness comprised of a 5μm piezoelectric PZT layer and a 1μm SiO_2 at the bottom of the beam structure. For the d_{33} mode device, the interdigitated electrodes were fabricated with 30μm widths and 30μm gaps. The proof mass for the d_{31} mode piezoelectric MEMS generator was fabricated under the beam structure with dimensions of 500×1500×500μm^3, and 750×1500×500μm^3 for the d_{33} mode. A different proof mass dimension comparing to the d_{31} mode piezoelectric MEMS generator was used to show readers how the proof masses influence the resonance frequency. Most of the process steps were undertaken in a standard clean room environment. The piezoelectric material PZT thin film deposition was deposited using aerosol deposition machine.

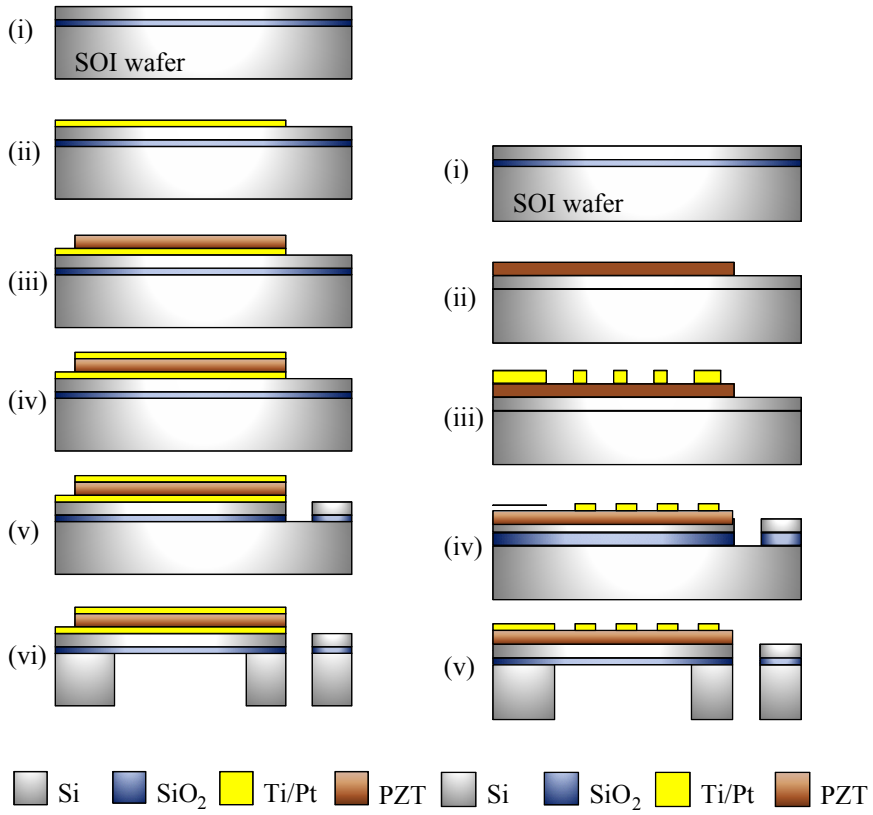

Figure 19. Fabrication processes of d_{31} (left) and d_{33} (right) devices

Figure 19 shows the fabrication process of both mode of the piezoelectric MEMS generator. SOI wafers with a 5μm device layer and a 1μm buried oxide layer was used in the process. The processes are similar to one another except for the second step, where the d_{31} generator has the bottom electrode deposited with a 30nm Ti and 220nm Pt on the top-side of the SOI wafer using an e-beam evaporator. PZT layers of 5μm were then deposited onto the bottom electrode of the d_{31} device, using the aerosol deposition method described above. For the d_{33} device the PZT layer is directly deposited upon the SOI wafer. The patterning processes required in the previous steps were done by lift-off processes. Then, the annealing process was taken place at a furnace of 650°C for 3 hours. Afterwards, an e-beam evaporator was used to deposit the top electrode with 30nm Ti and 220nm Pt and then patterned by lifting-off. The beam shape was defined and etched on the top side DRIE. The buried oxide layer was etched out using RIE at the same time. Finally a DRIE process was then used to etch the wafer from the back side until the beam was released. The proof mass was made at the same time and its size adjusted during the etching to the back side. The PZT layer was then poled under a high electric field. For the poling process, the device was heated up to 160°C using a

hot plate, followed by poling under 100V for 30 minutes, and then allowed to cool slowly to room temperature with the electric field applied through continuously during the entire heating and cooling process.

The SEM of the finished d_{31} and d_{33} modes piezoelectric MEMS generator are shown in figure 20 and figure 21. The cantilever beams were covered with laminated electrode and the proof mass at the tips can be seen. The beam structures could be seen to be bent upwards due to the thermal expansion difference for PZT and to the silicon wafer after the PZT cooled down to room temperature from 650°C.

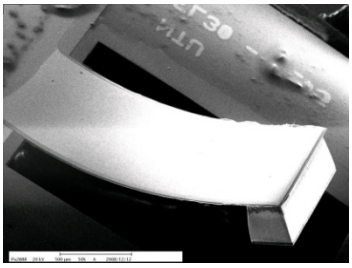

Figure 20. SEM photograph of a finished d_{31} mode device

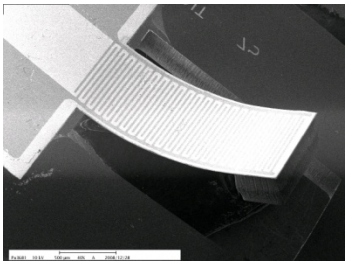

Figure 21. SEM photograph of a finished d_{33} mode device

4. Discussion on different types of MEMS power generators

4.1. Comparison between d31 and d33 mode piezoelectric MEMS generators

The d_{31} mode and the d_{33} mode piezoelectric MEMS generators were both excited at a 2g acceleration level. The measurement results are summarized in Table 3. The optimal load was found to be inversely proportional to the capacitance of the piezoelectric material [44, 45]. For the same dimensions of the beam shape of the d_{31} and d_{33} mode devices, it was obvious that the capacitance of the d_{31} mode device was larger than the d_{33} mode device. Therefore, the optimal resistive load for the d_{31} mode device was smaller than that of the d_{33} mode device. The output power for the d_{33} mode piezoelectric MEMS generator was smaller than that for the d_{31} mode piezoelectric MEMS generator. This was due to the PZT material of the d_{33} mode device which was poled by the interdigitated electrodes and which results in a non-uniform poling direction. The material under the electrodes was not used because it was not poled correctly. Furthermore, the further the distance from the surface of the PZT

material, the less effective the poling electric field strength will be. This causes an efficiency drop for the d_{33} mode piezoelectric MEMS generator when compared to the d_{31} mode piezoelectric MEMS generator. Nevertheless, the output voltage of the d_{33} mode piezoelectric MEMS generator was higher than that of the d_{31} mode piezoelectric MEMS generator and easily adjusted by the gap of the interdigitated electrodes under the same dimensions of the beam shape.

Mode	Resonant Frequency	Optimal Load	Power Output	Voltage Output (open circuit)	Voltage Output (with load)
d_{31}	255.9 Hz	150kΩ	2.099μW	2.415V_{P-P}	1.587V_{P-P}
d_{33}	214.0 Hz	510kΩ	1.288μW	4.127V_{P-P}	2.292V_{P-P}

Table 3. The Output performance of the d_{31} and d_{33} mode piezoelectric MEMS generators at 2g acceleration

5. Conclusion

In this chapter, the theoretical analysis, design and manufacture methods of two basic piezoelectric MEMS generators were introduced. For these piezoelectric MEMS generators, we investigated the relationship between output voltage and output power at different resistive loads.

The measurement results show that the d_{31} mode piezoelectric MEMS generator had a maximum open circuit output voltage of 2.675V_{P-P} and a maximum output power of 2.765μW with a 1.792V_{P-P} output voltage at resonant frequency of 255.9Hz at a 2.5g acceleration level. The d_{33} mode piezoelectric MEMS generator showed a maximum open circuit output voltage of 4.127V_{P-P} and a maximum output power of 1.288μW with a 2.292V_{P-P} output voltage at resonant frequency of 214Hz at a 2g acceleration level. The output power and the output voltage are also influenced by the driven acceleration intensely.

When comparing the output characteristics of both the d_{31} mode and the d_{33} mode piezoelectric MEMS generators, the results showed that the d_{31} mode device made of a PZT sandwiched between laminated electrodes was better in output power performance than the d_{33} mode device that composed of interdigitated electrodes at the top.

Author details

Wen Jong Wu* and Bor Shiun Lee
Department of Engineering Science and Ocean Engineering, National Taiwan University, Taipei, Taiwan

6. References

* Corresponding Author

[1] N. G. Elvin, A. A. Elvin and M. Spector. A self-powered mechanical strain energy sensor. Smart Materials & Structures. 2001;10 293-299
[2] J. M. Rabaey, M. J. Ammer, J. L. da Silva, D. Patel and S. Roundy. PicoRadio supports ad hoc ultra-low power wireless networking. Computer. 2000;33 42-48
[3] S. Roundy, P. K. Wright and J. Rabaey. A study of low level vibrations as a power source for wireless sensor nodes. Computer Communications. 2003;26 1131-1144
[4] R. Amirtharajah and A. P. Chandrakasan. Self-powered signal processing using vibration-based power generation. Ieee Journal of Solid-State Circuits. 1998;33 687-695
[5] S. Roundy, D. Steingart, L. Frechette, P. Wright and J. Rabaey. Power sources for wireless sensor networks. Wireless Sensor Networks, Proceedings. 2004;2920 1-17
[6] S. Roundy, E. S. Leland, J. Baker, E. Carleton, E. Reilly, E. Lai, B. Otis, J. M. Rabaey, P. K. Wright and V. Sundararajan. Improving power output for vibration-based energy scavengers. Ieee Pervasive Computing. 2005;4 28-36
[7] H. A. Sodano. A Review of Power Harvesting from Vibration Using Piezoelectric Materials. The Shock and Vibration Digest. 2004;36 197
[8] N. S. Shenck and J. A. Paradiso. Energy scavenging with shoe-mounted piezoelectrics. Ieee Micro. 2001;21 30-42
[9] G. K. Ottman, H. F. Hofmann and G. A. Lesieutre. Optimized piezoelectric energy harvesting circuit using step-down converter in discontinuous conduction mode. Ieee Transactions on Power Electronics. 2003;18 696-703
[10] N. N. H. Ching, H. Y. Wong, W. J. Li, P. H. W. Leong and Z. Y. Wen. A laser-micromachined multi-modal resonating power transducer for wireless sensing systems. Sensors and Actuators a-Physical. 2002;97-8 685-690
[11] M. El-hami, R. Glynne-Jones, N. M. White, M. Hill, S. Beeby, E. James, A. D. Brown and J. N. Ross. Design and fabrication of a new vibration-based electromechanical power generator. Sensors and Actuators a-Physical. 2001;92 335-342
[12] S. Meninger, J. O. Mur-Miranda, R. Amirtharajah, A. Chandrakasan and J. H. Lang. Vibration-to-electric energy conversion. Very Large Scale Integration (VLSI) Systems, IEEE Transactions on. 2001;9 64-76
[13] Y. Chiu and V. F. G. Tseng. A capacitive vibration-to-electricity energy converter with integrated mechanical switches. Journal of Micromechanics and Microengineering. 2008;18, 104004
[14] M. Miyazaki. Electric-Energy Generation through Variable-Capacitive Resonator for Power-Free LSI. IEICE - Transactions on Communications. 2004;87 549
[15] S. Roundy and P. K. Wright. A piezoelectric vibration based generator for wireless electronics. Smart Materials & Structures. 2004;13 1131-1142
[16] T. Starner. Human-powered wearable computing. Ibm Systems Journal. 1996;35 618-629
[17] L. Mateu and F. Moll. Optimum piezoelectric bending beam structures for energy harvesting using shoe inserts. Journal of Intelligent Material Systems and Structures. 2005;16 835-845
[18] L. Mateu and F. Moll. Appropriate charge control of the storage capacitor in a piezoelectric energy harvesting device for discontinuous load operation. Sensors and Actuators a-Physical. 2006;132 302-310

[19] S. Xu, Y. G. Wei, J. Liu, R. Yang and Z. L. Wang. Integrated Multilayer Nanogenerator Fabricated Using Paired Nanotip-to-Nanowire Brushes. Nano Letters. 2008;8 4027-4032

[20] P. J. Cornwell, J. Goethal, J. Kowko and M. Damianakis. Enhancing power harvesting using a tuned auxiliary structure. Journal of Intelligent Material Systems and Structures. 2005;16 825-834

[21] K. Mossi, C. Green, Z. Ounaies and E. Hughes. Harvesting energy using a thin unimorph prestressed bender: Geometrical effects. Journal of Intelligent Material Systems and Structures. 2005;16 249-261

[22] N. M. White, P. Glynne-Jones and S. P. Beeby. A novel thick-film piezoelectric micro-generator. Smart Materials & Structures. 2001;10 850-852

[23] H. S. Yoon, G. Washington and A. Danak. Modeling, optimization, and design of efficient initially curved piezoceramic unimorphs for energy harvesting applications. Journal of Intelligent Material Systems and Structures. 2005;16 877-888

[24] D. Guyomar, A. Badel, E. Lefeuvre and C. Richard. Toward energy harvesting using active materials and conversion improvement by nonlinear processing. Ultrasonics, Ferroelectrics and Frequency Control, IEEE Transactions on. 2005;52 584-595

[25] E. Lefeuvre, A. Badel, A. Benayad, L. Lebrun, C. Richard and D. Guyomar. A comparison between several approaches of piezoelectric energy harvesting. Journal De Physique Iv. 2005;128 177-186

[26] E. Lefeuvre, A. Badel, C. Richard, L. Petit and D. Guyomar. A comparison between several vibration-powered piezoelectric generators for standalone systems. Sensors and Actuators a-Physical. 2006;126 405-416

[27] E. Lefeuvre, A. Badel, C. Richard and D. Guyomar. Piezoelectric energy harvesting device optimization by synchronous electric charge extraction. Journal of Intelligent Material Systems and Structures. 2005;16 865-876

[28] A. Badel, D. Guyomar, E. Lefeuvre and C. Richard. Efficiency enhancement of a piezoelectric energy harvesting device in pulsed operation by synchronous charge inversion. Journal of Intelligent Material Systems and Structures. 2005;16 889-901

[29] Y. C. Shu, I. C. Lien and W. J. Wu. An improved analysis of the SSHI interface in piezoelectric energy harvesting. Smart Materials & Structures. 2007;16 2253-2264

[30] Y. B. Jeon, R. Sood, J. H. Jeong and S. G. Kim. MEMS power generator with transverse mode thin film PZT. Sensors and Actuators a-Physical. 2005;122 16-22

[31] H. B. Fang, J. Q. Liu, Z. Y. Xu, L. Dong, D. Chen, B. C. Cai and Y. Liu. A MEMS-based piezoelectric power generator for low frequency vibration energy harvesting. Chinese Physics Letters. 2006;23 732-734

[32] H. B. Fang, J. Q. Liu, Z. Y. Xu, L. Dong, L. Wang, D. Chen, B. C. Cai and Y. Liu. Fabrication and performance of MEMS-based piezoelectric power generator for vibration energy harvesting. Microelectronics Journal. 2006;37 1280-1284

[33] D. Shen, J. H. Park, J. Ajitsaria, S. Y. Choe, H. C. Wikle and D. J. Kim. The design, fabrication and evaluation of a MEMS PZT cantilever with an integrated Si proof mass for vibration energy harvesting. Journal of Micromechanics and Microengineering. 2008;18, 055017

[34] M. Marzencki, Y. Ammar and S. Basrour. Integrated power harvesting system including a MEMS generator and a power management circuit. Sensors and Actuators a-Physical. 2008;145 363-370

[35] J.-Q. Liu, H.-B. Fang, Z.-Y. Xu, X.-H. Mao, X.-C. Shen, D. Chen, H. Liao and B.-C. Cai. A MEMS-based piezoelectric power generator array for vibration energy harvesting. Microelectronics Journal. 2008;39 802-806

[36] J. Ajitsaria, S. Y. Choe, D. Shen and D. J. Kim. Modeling and analysis of a bimorph piezoelectric cantilever beam for voltage generation. Smart Materials & Structures. 2007;16 447-454

[37] A. Erturk and D. J. Inman. Comment on 'modeling and analysis of a bimorph piezoelectric cantilever beam for voltage generation'. Smart Materials & Structures. 2008;17, 058001

[38] N. E. duToit, B. L. Wardle and S. G. Kim. Design considerations for MEMS-scale piezoelectric mechanical vibration energy harvesters. Integrated Ferroelectrics. 2005;71 121-160

[39] N. E. duToit and B. L. Wardle. Performance of microfabricated piezoelectric vibration energy harvesters. Integrated Ferroelectrics. 2006;83 13-32

[40] B. M. Xu, Y. H. Ye, L. E. Cross, J. J. Bernstein and R. Miller. Dielectric hysteresis from transverse electric fields in lead zirconate titanate thin films. Applied Physics Letters. 1999;74 3549-3551

[41] X. Y. Wang, C. Y. Lee, Y. C. Hu, W. P. Shih, C. C. Lee, J. T. Huang and P. Z. Chang. The fabrication of silicon-based PZT microstructures using an aerosol deposition method. Journal of Micromechanics and Microengineering. 2008;18, 055034

[42] X.-Y. Wang, C.-Y. Lee, C.-J. Peng, P.-Y. Chen and P.-Z. Chang. A micrometer scale and low temperature PZT thick film MEMS process utilizing an aerosol deposition method. Sensors and Actuators A: Physical. 2008;143 469-474

[43] Y. C. Shu and I. C. Lien. Efficiency of energy conversion for a piezoelectric power harvesting system. Journal of Micromechanics and Microengineering. 2006;16 2429-2438

[44] Y. C. Shu and I. C. Lien. Analysis of power output for piezoelectric energy harvesting systems. Smart Materials & Structures. 2006;15 1499-1512